NASA
Technical
Paper
2823

July 1988

Three-Dimensional Analysis of a Postbuckled Embedded Delamination

John D. Whitcomb

NASA

NASA
Technical
Paper
2823

1988

Three-Dimensional Analysis of a Postbuckled Embedded Delamination

John D. Whitcomb
Langley Research Center
Hampton, Virginia

National Aeronautics
and Space Administration

**Scientific and Technical
Information Division**

Abstract

Delamination growth caused by local buckling of a delaminated group of plies was investigated. Delamination growth was assumed to be governed by the strain-energy release rates G_I, G_{II}, and G_{III}. The strain-energy release rates were calculated using a geometrically nonlinear, three-dimensional, finite element analysis. The program is described and several checks of the analysis are discussed. Based on a limited parametric study, the following conclusions were reached:

1. The problem is definitely mixed-mode. In some cases G_I is larger than G_{II}; for other cases the opposite is true.
2. In general, there is a large gradient in the strain-energy release rates along the delamination front.
3. The locations of maximum G_I and G_{II} depend on the delamination shape and the applied strain.
4. The mode III component was negligible for all cases considered.
5. The analysis predicted that parts of the delamination would overlap. The results presented herein did not impose contact constraints to prevent overlapping. Further work is needed to determine the effects of allowing the overlapping.

Introduction

Composite materials exhibit a number of different failure mechanisms. Among these are delamination, fiber breakage, and intralaminar cracking. In addition to the failure mechanisms operative under tensile loads, there are mechanisms related to instability, such as fiber microbuckling and buckling of a group of delaminated laminae, which can be important under compression loads. Delamination which is driven by local buckling of a group of laminae is discussed in this report. This mechanism is referred to herein as instability-related delamination growth (IRDG). The magnitudes of the modes of strain-energy release rates G_I, G_{II}, and G_{III} are often used to predict when delamination will occur. It is assumed that G_I, G_{II}, and G_{III} are the critical parameters for predicting delamination growth.

Figure 1 shows two configurations which exhibit IRDG, laminates with a through-width or an embedded delamination. The through-width delamination has been analyzed using a variety of detailed and approximate stress analyses (refs. 1 to 6). Experimental measurements of IRDG have been published for static loads (refs. 6 to 9) and fatigue loads (refs. 1, 3, 7, and 8). The through-width delamination is perhaps the simplest configuration that exhibits IRDG. Hence, it provides a convenient vehicle for evaluating various ideas about testing and analysis.

The embedded-delamination configuration has also been studied both analytically (refs. 10 to 15) and experimentally (refs. 7, 12, and 16 to 18). To date, however, there have been no detailed analyses of the embedded delamination. The analyses have been limited to Rayleigh-Ritz or finite element plate analysis. With one exception (ref. 14), only average total strain-energy release rates along the delamination front have been presented. In reference 14, the distribution of total strain-energy release rate was calculated. A geometrically nonlinear, three-dimensional, finite element analysis (or some other numerical technique) is required to calculate the individual modes of strain-energy release rate. However, three-dimensional finite element analysis tends to be very expensive. Since nonlinear analysis requires iteration, it is even more expensive. This expense probably explains the lack of detailed analysis for this configuration in the literature. However, until detailed analyses are performed, the accuracy of approximate analyses cannot be assessed.

There are two objectives to this paper. The first is to describe the three-dimensional, geometrically nonlinear, finite element program which was developed for this study. The program is named NONLIN3D. The second objective is to show the effect of several parameters on the magnitude and distribution of the strain-energy release rates. The parameters considered were delamination shape, delamination size, and strain level.

Symbols

a, b	semi-axes of elliptical delamination in x- and y-directions, respectively
a_i, b_i, c_i, d_i, a_i', b_i', c_i', d_i'	nodes used in calculation of strain-energy release rates
C_{ij}	constitutive coefficients
$\overline{C}_{ij}$	constitutive coefficients for a "homogeneous quasi-isotropic laminate"
E_{11}, E_{22}, E_{33}	Young's moduli for orthotropic material
F^α	nodal forces
G	strain-energy release rate

G_I, G_{II}, G_{III}, G_T	mode I, mode II, mode III, and total strain-energy release rates
G_{12}, G_{23}, G_{13}	shear moduli for orthotropic material
H	thickness of base laminate
h	thickness of sublaminate
$K^{\alpha\beta}$	coefficients in tangential stiffness matrix
P	transverse load
q^α	nodal displacements
S	perimeter coordinate
U	strain energy
u, v, w	displacements in x-, y-, and z-directions
V	volume
W	width of finite element model
w_o	transverse displacement in center of plate
x, y, z	rectangular Cartesian coordinates in global coordinate system
x', y', z'	rectangular Cartesian coordinates in local coordinate system
Δa	increment in delamination length
ε_j	strains
ε_x	strain in x-direction
ν_{12}, ν_{23}, ν_{13}	Poisson's ratios for orthotropic material
Π	total potential energy

Analysis

The theoretical aspects of NONLIN3D, the geometrically nonlinear, three-dimensional, finite element program used for this study, are discussed in this section. In particular, the following topics are covered:

1. Governing nonlinear equations
2. Substructuring
3. Calculation of strain-energy release rate

After the discussion of NONLIN3D, the mesh generation and the finite element models are discussed. The material properties are also described.

Governing Nonlinear Equations

The derivation of the equilibrium equations and the expressions for the internally generated nodal forces and the tangent stiffness matrix are discussed in this subsection. The strain-displacement relations are also discussed.

The total potential energy is given by

$$\Pi = \frac{1}{2}\int C_{ij}\varepsilon_i\varepsilon_j dV - F^\alpha q^\alpha \tag{1}$$

where the integral term is the strain energy and the second term is the potential energy of the applied loads. The terms C_{ij} and ε_i are terms in the constitutive matrix and the strains, respectively. The terms F^α and q^α are the generalized forces and displacements, respectively. The adjective "generalized" is used to indicate that F^α and q^α need not be forces and displacements in the usual sense. For example, in traditional Rayleigh-Ritz analyses, the unknowns q^α are simply coefficients in the series expansion for the displacements. In this discussion, however, F^α and q^α always refer to the nodal forces and displacements in the x-, y-, and z-directions. The system is assumed to be conservative; hence, the equilibrium state is obtained by minimizing Π, which is accomplished by setting the first partial derivatives with respect to the unknowns equal to zero:

$$\frac{\partial \Pi}{\partial q^\alpha} = \int C_{ij}\varepsilon_i \frac{\partial \varepsilon_j}{\partial q^\alpha}\, dV - F^\alpha = 0 \tag{2}$$

Equation (2) is nonlinear because of the nonlinear strain-displacement relations. The integral in equation (2) gives the magnitude of the internally generated nodal forces corresponding to the current displacements. Until a converged solution is obtained, the internally generated forces do not equal the externally applied forces. The differences in the forces, referred to as residuals, equal $\frac{\partial \Pi}{\partial q^\alpha}$. The Newton-Raphson procedure that was used to solve equation (2) requires the partial derivatives of the residuals with respect to the unknowns. These partial derivatives of the residuals are the coefficients in the tangential stiffness matrix K and are given by

$$K^{\alpha\beta} = \frac{\partial^2 \Pi}{\partial q^\alpha \partial q^\beta} = \int C_{ij}\, \frac{\partial \varepsilon_i}{\partial q^\alpha}\, \frac{\partial \varepsilon_j}{\partial q^\beta}\, dV + \int C_{ij}\, \frac{\partial^2 \varepsilon_i}{\partial q^\alpha \partial q^\beta}\, dV \tag{3}$$

The first and second integrals give the terms in the large displacement and geometric stiffness matrices, respectively. If the strains are equal to zero, the large displacement matrix obtained using the first integral and the nonlinear strain-displacement relations is identical to the matrix obtained by simply updating the coordinates and using the linear strain-displacement relations. If the strains are not equal to zero, there is a difference. This difference was verified numerically for 2-D elements.

A Lagrangian formulation is used for NONLIN3D. For infinitesimal strain, the nonlinear strain-displacement relations (ref. 19) are

$$\left.\begin{aligned}
\varepsilon_1 &= u_x + 1/2(u_x u_x + v_x v_x + w_x w_x) \\
\varepsilon_2 &= v_y + 1/2(u_y u_y + v_y v_y + w_y w_y) \\
\varepsilon_3 &= w_z + 1/2(u_z u_z + v_z v_z + w_z w_z) \\
\varepsilon_4 &= u_y + v_x + (u_x u_y + v_x v_y + w_x w_y) \\
\varepsilon_5 &= v_z + w_y + (u_z u_y + v_z v_y + w_z w_y) \\
\varepsilon_6 &= u_z + w_x + (u_z u_x + v_z v_x + w_z w_x)
\end{aligned}\right\} \quad (4)$$

where u, v, and w are displacements in the x-, y-, and z-directions, and the subscripts x, y, and z indicate partial differentiation (e.g., $u_y = \frac{\partial u}{\partial y}$). The nodal values of u, v, and w are the unknowns referred to previously as q^α. Note that ε_4, ε_5, and ε_6 are engineering shear strains. Since a Lagrangian formulation is used, the strains are based on the original configuration. For example, ε_1 is the axial strain of a line which was originally (i.e., before deformation) parallel to the x-axis. Although this line could be oriented parallel to the y-axis after deformation, the axial strain is still ε_1 and not ε_2.

Substructuring

The program NONLIN3D was designed to perform analysis by substructures. A brief description of the substructuring technique is given here. More details can be found in reference 20. In addition to reducing computer memory requirements, substructuring allows the structure to be modeled as a combination of linear and nonlinear components. For the configurations studied herein (fig. 1), linear analysis is appropriate everywhere except the majority of the postbuckled region. By substructuring into linear and nonlinear regions, expensive iterative solution is needed for only a fraction of the equations.

In the current study, two substructures are used: one linear and one nonlinear. The procedure begins by obtaining a reduced stiffness matrix and load vector for the linear region. The reduced stiffness matrix can be treated as the stiffness matrix for just another type of element. Because of the large number of nodes, this element is referred to as a superelement. The stiffness matrix and load vector are "reduced" in the sense that only the nodes shared by the two substructures (the interface nodes) are included.

The technique used for calculating the reduced stiffness coefficients utilized the formal definition of a stiffness coefficient: a stiffness coefficient is related to the restraint forces required to maintain unit displacement at one degree of freedom (DOF) and zero displacement at the remainder of the element DOF's. Suppose there are to be n DOF's in the superelement. These n DOF's are restrained. One of these DOF's is specified to have a unit displacement (and there are no other loads) and the governing equations are solved. The restraint forces at all n DOF's constitute one column of the reduced stiffness matrix. This procedure is repeated for all n DOF's. The reduced load vector is obtained in a similar fashion. All n DOF's in the superelement are still restrained. However, the specified loads for the linear region are now applied. The reduced load vector is equal to the negative of the restraint forces at the restrained nodes.

Once the superelement stiffness matrix and load vector are calculated, the analysis proceeds to the nonlinear substructure. Whenever the nonlinear stiffness matrix and load vector are formed, the interaction with the linear substructure is included by simply adding the superelement stiffness matrix and load vector. When the internally generated nodal forces are calculated to determine residuals, the contribution of the linear substructure consists of the product of the superelement stiffness matrix and the superelement nodal displacements.

For the configuration analyzed, the delamination front is within the linear substructure. Hence, further work is required even after obtaining a converged solution for the nonlinear substructure. After obtaining a converged solution, the displacements for the interface nodes are known. These displacements fully account for the effect of the nonlinear substructure on the linear substructure. That is, the displacements in the linear substructure can be determined as though there were no other substructure, except that the magnitudes of the displacements at the interface nodes are specified. To reduce the computer resource requirements, it is usually advantageous to obtain multiple solutions for the nonlinear substructure and then obtain multiple solutions for the linear substructure.

Strain-Energy Release Rate Calculation

The well-known virtual crack closure technique (ref. 21) served as the basis of the strain-energy

release rate calculation. This procedure determines G_I, G_{II}, and G_{III} from the energy required to close the delamination over a short distance Δa. The closure energy involves products of delamination front nodal forces and relative displacements behind the delamination front. The delamination front nodal forces can be determined by actually closing the delamination over Δa. Another technique, which requires only a single solution, assumes that the current delamination front nodal forces are the same as they would be if the delamination length were reduced by Δa. The single-solution method was used herein.

Figure 2 is a schematic of the delamination front region. The nodes of interest for the strain-energy release rate calculations are indicated by the filled circles. Because it is not appropriate to close the delamination over part of an element, there are four sets of nodes (indicated by the letters a, b, c, and d) which are used to calculate the closure energies. The relative displacements are obtained by subtracting the displacements at nodes a_i' and b_i' from the displacements at nodes a_i and b_i, respectively. The forces are equal to the nodal forces transmitted across the delamination plane at nodes c_i and d_i. These forces are obtained by evaluating the integral $\int C_{ij}\varepsilon_i \frac{\partial \varepsilon_j}{\partial q^\alpha}\, dV$ for all elements which are connected to nodes c_i or d_i and whose centroids lie above the delamination plane. There are two sets of energy products. One of the sets of energy products consists of the relative displacements for nodes a_i and a_i' multiplied by the forces for nodes c_i. The other set of energy products consists of the relative displacements for nodes b_i and b_i' multiplied by the forces for nodes d_i. The energies equal half of these products.

Strain-energy release rate is a measure of energy per unit area. Hence, the energy products must be normalized by the appropriate areas. Unfortunately, there is not a simple exact way to determine the appropriate areas. The primary complication is that the midside nodes and corner nodes are "weighted" differently by the assumed element shape functions. The result is that, even if the strain-energy release rates were actually constant along the delamination front, there would be much larger energy products for the midside nodes than for the corner nodes. For example, in figure 2 the energy products associated with nodes c_2 and c_4 would be much larger than for those associated with nodes c_1 and c_3. An approximate solution to this dilemma is as follows. The strain-energy release rate is not calculated for locations like c_2 and c_4 along the delamination front. Instead, the energy products associated with these locations are split evenly between the adjacent nodes. For example, the energy associated with location c_3 along the delamination front becomes

$$\overline{E} = \overline{E}_{a_3 a_3' c_3} + \overline{E}_{b_2 b_2' d_2} + \frac{1}{2}\left(\overline{E}_{a_2 a_2' c_2} + \overline{E}_{a_4 a_4' c_4}\right) \tag{5}$$

where $\overline{E}$ denotes the energy products associated with G_I, G_{II}, and G_{III}, and the subscripts indicate the nodes involved. The area is approximated by the product of Δa times the distance between the midside nodes on either side of the corner node being considered. For example, the area for node c_3 is Δa times the distance from node c_2 to node c_4.

If the delamination front is not parallel to one of the coordinate axes, it is preferable to add a coordinate transformation to the procedure outlined above. In particular, a local coordinate system is defined for each node along the physical delamination front (i.e., the c_i nodes). Figure 3 is a schematic of a delamination plane and the global (xy) and local $(x'y')$ coordinate systems. This local coordinate system has one axis tangent to the delamination front, one axis normal to the delamination front, and one axis normal to the delamination plane. For all the cases considered, z and z' were parallel. The transformed nodal forces $F_{x'}$, $F_{y'}$, and $F_{z'}$ are defined as

$$\left.\begin{aligned} F_{x'} &= F_x \cos\theta + F_y \sin\theta \\ F_{y'} &= -F_x \sin\theta + F_y \cos\theta \\ F_{z'} &= F_z \end{aligned}\right\} \tag{6}$$

The relative displacements are transformed similarly. The transformed forces and relative displacements are then used to calculate the energy products. Figure 3 also defines the perimeter coordinate S, which is the distance along the delamination front measured from the y-axis.

The procedure just outlined was implemented in two slightly different ways for the results presented here. The difference was in the way the nodal forces were calculated. Initially in the study, the nonlinear strain-displacement relations were used to calculate the nodal forces from the nodal displacements in the linear region. This is inconsistent, but if the region assumed to be linear is "exactly linear," it makes no difference. The results for the mesh convergence study were obtained using this procedure. All the other results were obtained by using the linear strain-displacement relations to calculate the nodal forces from the nodal displacements in the linear region. Because the linear region is not exactly linear, there is a difference in the results obtained using the two methods. The configuration used for the mesh

convergence study was also used in the parametric study, so results appear for that configuration using both methods. The second method is recommended by the author.

Mesh Generation and Typical Model

Figure 4 is an outline of the procedure used for mesh generation. This procedure is based on the procedure in reference 22. A two-dimensional model is swept through a 90° arc to generate a cylindrical 3-D mesh. The outer part of the cylindrical mesh is then transformed to obtain a square boundary. Then an elliptical transformation is applied to obtain an elliptical delamination front. If the ellipse is longer in the y-direction than in the x-direction (i.e., $b > a$), the conformal transformation is

$$\left.\begin{aligned} x' &= x \\ y' &= y\sqrt{1+\frac{b^2-a^2}{x^2+y^2}} \\ z' &= z \end{aligned}\right\} \tag{7}$$

If $a > b$, the transformation is the same except that x and y are interchanged. To avoid a singularity in equation (7), nodes at zero radius were shifted to lie on an arc of very small radius, about 10^{-9} m.

The transformation in equation (7) maintains the orthogonality of lines which were orthogonal in the modified cylindrical mesh (fig. 4). This orthogonality at the delamination front simplifies the pairing of nodal forces and relative displacements in the strain-energy release-rate calculation.

A peculiarity of the transformation in equation (7) is the unusually close spacing of the elements close to the delamination front on the long axis of the ellipse. Figures 5(a) and 5(b) show the mesh before and after the transformation. Also, there appears to be a triangular element in figure 5(c). This element has two sides which are essentially collinear. A modified transformation which results in more even mesh refinement is obtained by introducing a scale factor for the "stretching" as follows:

$$y' = y\left(\sqrt{1+\frac{b^2-a^2}{x^2+y^2}}F - F + 1\right) \tag{8}$$

where

$$F = \frac{\sqrt{x^2+y^2}}{r} \text{ for } r \geq \sqrt{x^2+y^2}$$

and

$$F = 1 \text{ for } r \leq \sqrt{x^2+y^2}$$

By making the parameter r a little less than the radius of the delamination front in the cylindrical mesh, orthogonality is maintained in the neighborhood of the delamination front during the elliptical transformation.

After the elliptical transformation, the midside nodes are no longer at the middle of an element edge. Therefore, the coordinates of the midside nodes are recalculated as the average of the coordinates of the adjacent corner nodes.

Figure 6 shows a typical finite element model. The elements are 20-node isoparametric hexahedrons. Because of symmetry it is sufficient to model only one fourth of the specimen and impose the constraints $u = 0$ on $x = 0$ and $v = 0$ on $y = 0$. There is also a constraint $w = 0$ on $z = 0$. This constraint was imposed to remove global bending from the analysis. In reality, there might be global bending (particularly if the buckled region is thick), but the amount of global bending depends on the region modeled and the boundary conditions at the external boundaries. Imposition of $w = 0$ on $z = 0$ simply removes overall specimen size and external boundary conditions as parameters to be considered in this study. The constraint on w represents a laminate which is well constrained globally. Of course, the imposition $w = 0$ on $z = 0$ could also be viewed as an indication of symmetry about the $z = 0$ plane. This view implies the presence of two delaminations.

Along the boundary $x = W$, all u displacements are specified to equal $W\varepsilon_x$, where ε_x is the specified compressive axial strain. To initiate transverse deflections, a transverse load was applied at the center of the delaminated region. After a converged solution was obtained, the load was removed, and solutions were obtained with only compression loading.

Figure 7 shows a typical model after division into substructures. Most of the postbuckled region is included in the nonlinear substructure. The distance between the delamination front and the beginning of the nonlinear substructure was ℓ. In all cases, ℓ was approximately equal to the sublaminate thickness h. To check the validity of the substructuring, a crude model was analyzed with and without substructuring. The strain-energy release rates were negligibly different. For all the cases considered, the sublaminate thickness h and base laminate thickness H were 0.4 and 4 mm, respectively.

Material Properties

The objective of this paper is to consider only the effect of geometric parameters on G_I, G_{II}, and G_{III}. Consequently, material properties were chosen to minimize the effect of material properties on the variations in G_I, G_{II}, and G_{III}. For quasi-isotropic

laminates, the in-plane stiffness is independent of the orientation in the xy plane. However, even for quasi-isotropic laminates, the flexural stiffness varies with orientation. Hence, even if the postbuckled region consisted of a quasi-isotropic group of plies, variations would be expected in the strain-energy release rate along the delamination front solely because of the variation in flexural stiffness. Also, the properties of the plies on either side of the delamination would be expected to at least affect the percentages of G_I, G_{II}, and G_{III}.

The simplified material properties chosen for this study are those for a "homogeneous quasi-isotropic laminate" throughout the entire specimen (buckled and unbuckled regions). These properties $\overline{C}_{ij}$ are obtained as follows:

$$\overline{C}_{ij} = \frac{1}{8}\sum_{k=1}^{8}(C_{ij})^k \tag{9}$$

where $(C_{ij})^k$ are the constitutive properties for the k^{th} ply in the 8-ply quasi-isotropic laminate $(\pm 45/0/90)_s$. With these properties throughout, there are obviously no stacking sequence effects and there is no variation of material properties with orientation.

The lamina properties used to calculate C_{ij} were selected to be typical of graphite/epoxy (ref. 23). The moduli and Poisson's ratios are as follows:

$$\left.\begin{aligned} E_{11} &= 134 \text{ GPa} \\ E_{22} = E_{33} &= 10.2 \text{ GPa} \\ G_{12} = G_{13} &= 5.52 \text{ GPa} \\ G_{23} &= 3.43 \text{ GPa} \\ \nu_{12} = \nu_{13} &= 0.3 \\ \nu_{23} &= 0.49 \end{aligned}\right\} \tag{10}$$

Results and Discussion

The results of the analysis evaluation and parametric study are described in this section. The analysis evaluation has several parts. First, the results for a transversely loaded laminate are discussed. This configuration was selected as a check case because it exhibits geometric nonlinearity and a closed-form plate solution is available. Then the results of the mesh convergence and allowable residual studies are discussed. Finally, the results of a limited parametric study are discussed.

Transversely Loaded Plate

A closed-form solution for a circular isotropic plate subjected to a central point load is given in reference 24. This solution is exact for linear deflections and approximate for large deflections. The equation for the central deflection w_o is

$$\frac{w_o}{h} + 0.443\left(\frac{w_o}{h}\right)^3 = 0.217\frac{Pa^2}{Eh^4} \tag{11}$$

Finite element analyses were performed using a mesh similar to that in figure 6, but with a circular debond. The thickness and radius of the debonded region were 0.4 mm and 15 mm, respectively. The Young's modulus E was 207 GPa, and the Poisson's ratio was 0.3.

Figure 8(a) compares the deflection at the center obtained from the closed-form solution with that of NONLIN3D. The agreement between the two analyses is excellent in the linear and initial nonlinear regions. There is a 10-percent difference in the two curves at the highest load level considered. This difference is not surprising, since the closed-form analysis is not exact for large deflections.

The closed-form solution in reference 24 can be used to calculate the total strain-energy release rate. Because the configuration is axisymmetric, G_T is constant around the boundary. The strain-energy release rate is $-(\partial U/\partial a)/(2\pi a)$. The strain energy U can be calculated as the work done by the applied load (since all the work is stored as strain energy) as follows:

$$U = \int P\, dw_o \tag{12}$$

Equation (12) yields

$$U = 2.30\frac{w_o^2 Eh^3}{a^2} + 0.510\frac{w_o^4 Eh}{a^2} \tag{13}$$

An expression for G_T is obtained by differentiating equation (13) with respect to a and dividing by the circumference as follows:

$$G_T = \frac{Ehw_o^2}{2\pi a^4}\left(\frac{h^2}{0.217} + 1.02w_o^2\right) \tag{14}$$

Figure 8(b) shows G_T plotted against load. Results are shown for the linear closed-form solution (eq. (14) without the fourth-order w_o term), the nonlinear closed-form solution (eq. (14)), and NONLIN3D. The results are plotted with log-log axes because of the wide range of the parameters. In the linear range, all three solutions agree very well. Even after nonlinear effects become important, the nonlinear closed-form solution and NONLIN3D agree very well.

These comparisons indicate that NONLIN3D does account for geometric nonlinearity and that the technique for the strain-energy release-rate calculation is valid.

Mesh Refinement

Several configurations were analyzed as part of this study. Consequently, it was neither practical nor warranted to perform a convergence study for all cases. Instead, a systematic convergence study was performed for a single configuration. Mesh refinements for other configurations were selected based on the results of the convergence study.

The configuration selected for the convergence study had a circular delamination with a radius of 15 mm. The sublaminate thickness h was 0.4 mm and the base laminate thickness H was 4 mm. The overall laminate width W was 50 mm. The material properties were those for the homogeneous quasi-isotropic laminate described previously. Figure 9 shows the extremes of refinement used for the 2-D meshes. The elements in the coarse mesh were subdivided to obtain the refined mesh. For the coarse mesh, only two elements were used to model most of the buckled region. As described previously, the 2-D meshes were swept through a 90° arc to generate the 3-D meshes. Figure 10 shows four of the meshes generated. As shown in the figure, the number of slices of elements was also varied. Models with 4 and 8 slices are shown; a 12-slice model was also used. Information on all the models used in the convergence study is given in table 1. As shown by the figures and the table, a fairly wide range of refinement was examined.

Since strain-energy release rates were of primary importance, variations in G_I, G_{II}, and G_{III} were used to determine the adequacy of the mesh refinement. Figure 11 shows the distribution of G_I and G_{II} along the delamination front for three strain levels and four models (models 1, 3, 4, and 6). Only symbols are shown for the crudest mesh, model 3. These meshes bracket the entire range of refinement in table 1. The mode III component G_{III} was negligible for all cases. Of interest here are the differences in the results obtained using the various meshes. Except for model 3, which only had 4 slices of elements, the results from all the models are essentially equal. Even a coarse 4-slice model gives the correct trends. Apparently, a fairly crude model is sufficient to calculate G_I and G_{II}. The significance of the magnitude and the distribution of G_I and G_{II} is discussed subsequently.

Allowable Residual

The program NONLIN3D solves the governing nonlinear equations by using a modified Newton-Raphson solution procedure. During each iteration, the internally generated forces are compared with the externally applied loads. The differences are the residuals. If all the residuals are identically zero, the governing equations are exactly satisfied. Of course, in practice, exact agreement is seldom obtained. Iteration could continue until the algorithm's best approximation of zero is obtained. The size of this "numerical" zero depends on the computer and the type specifications in the program. However, negligible residuals are, in general, orders of magnitude larger than a numerical zero.

To determine what is a negligible residual, three residual tolerances were considered: 1000 N, 1 N, and 0.0001 N. A laminate with a 30 × 60 mm delamination was analyzed for five strain levels. The range of strains was such that the maximum lateral deflection for the buckled region varied from about 0.6 to 2.2 times the thickness of the buckled region. The tolerance of 1000 N gave erroneous results. The other two tolerances gave virtually identical results except for the lowest strain level ($\varepsilon_x = -0.001$), for which there were differences of about 6 percent. Figure 12 shows G_I and G_{II} for $\varepsilon_x = -0.001$ (i.e., the worst case). Results for the other strains are not shown, since the differences are very small.

Based on these results, a tolerance of 0.0001 N was selected for all the analyses. A somewhat larger residual could probably have been tolerated. However, the residuals tend to decrease quite rapidly during the iterations, so there is little to be gained (in terms of reduced cost) by trying to specify the largest acceptable residual. Also, a larger tolerance might give poor results for some cases in which the loads are small.

Parametric Study

The parameters considered were strain level, delamination shape, and delamination size. First, the deformation of the postbuckled region is discussed. Then the calculated strain-energy release rates are presented.

Figure 13 shows lateral displacement in the middle of the delaminated region plotted against axial strain for two circular and two elliptical delaminations. The dimensions of the delaminations are shown in the figure. The curves indicate that when the buckling load is exceeded, the displacement increases rapidly at first with increased strain. Then the rate of increase in displacement decreases. Obviously, the response is quite nonlinear.

Figure 14 shows deformed finite element meshes for a circular and an elliptical delamination. The displacements have been multiplied by 10 to improve visualization. The deformed shape is relatively simple except near the delamination front. For both cases, the delamination front is open near the y-axis. However, for the circular delamination, the delamination faces actually overlap near the x-axis (i.e.,

near the $y = 0$ plane). Even at strains smaller and larger than those shown, the circular delamination exhibited overlapping. For the elliptical delamination, "small" strains result in opening of the delamination along the entire length. At larger strains (not shown), the elliptical delamination also exhibited overlapping. Strictly speaking, constraints should be added to prevent overlapping of the delamination faces. However, including constraints to prevent overlapping further complicates an already complicated stress analysis problem. Consequently, no contact constraints were added for any of the results presented in this paper. In the results that follow (figs. 15 to 17), dashed lines are used for the G_I and G_{II} distribution curves in regions where overlap occurred.

Figure 15 shows the G_I and G_{II} distributions for a circular delamination for five strain levels. This is the same configuration used for the convergence study. The G_{III} distribution was essentially zero for this and all other cases considered in this study. In general, G_{III} would not necessarily be expected to be zero. The strain-energy release rates are plotted in figure 15 using the perimeter coordinate S. This coordinate is zero where the delamination front meets the y-axis and is maximum where the delamination front meets the x-axis. Both G_I and G_{II} show large variations along the front and are largest at $S = 0$. There is overlapping of the delamination surfaces over a large portion of the front, as indicated in figure 15(a). Although G_I is larger than G_{II} for the five strain levels, the difference is not large; this is definitely a mixed-mode situation. Since both G_I and G_{II} are largest at $S = 0$, delamination growth would be expected to occur preferentially perpendicular to the load direction, that is, in the y-direction.

Since a circular delamination is expected to become elongated perpendicular to the load direction, a 30 × 60 mm elliptical delamination was analyzed. Figure 16 shows the distribution of G_I, G_{II}, and G_T for this elliptical delamination. There is a large variation of both G_I and G_{II} along the front. Note that the location of the G_I peak shifts slightly with strain level. In contrast to the circular delamination, the peak values of G_I and G_{II} occur at different locations. Also, the peak value of G_{II} is larger than the peak value of G_I, except for the case $\varepsilon_x = -0.005$. The total strain-energy release rate (fig. 16(c)) varies significantly along the front for the larger strains, but for the smaller strains the magnitude is almost constant. Depending on the choice of growth criterion, very different predictions of even the direction of growth are possible. A criterion based only on G_I would predict growth perpendicular, or nearly perpendicular, to the load direction for all the strain levels. A criterion based only on G_{II} would predict growth parallel to the load direction. For the smallest strains, a criterion based on total strain-energy release rate would predict almost uniform growth along the delamination front.

Figure 17 shows G_I and G_{II} for a 60 × 60 mm delamination. Comparison of figures 15 and 17 shows the effect of delamination size on G_I and G_{II} for two circular delaminations. Both delaminations were subjected to the same strain levels. Figures 15(a) and 17(a) show that the larger delamination is closed (actually overlapping) over more of the delamination front. Also, the distribution in the overlapping region is more complicated for the larger delamination. This is because the strains for the larger delamination are larger multiples of the bifurcation buckling strain. This conclusion was verified by subjecting the smaller delamination to higher strains. (These results are not presented in this report.) The larger delamination has a much larger G_I for the region near $S = 0$. Figures 15(b) and 17(b) show that G_{II} is also larger for the larger delamination near $S = 0$. Hence, unstable extension of the delamination might be expected once it begins to grow. However, based on the calculated strain-energy release rates, a circular delamination is not expected to grow self-similarly into a larger circular delamination. It should become elliptical.

Figures 15 and 16 show results for 30 × 30 and 30 × 60 mm delaminations. Comparison of figures 15 and 16 shows that, except for the lowest strains, the smaller (circular) delamination actually has a larger G_I. Hence, the growth rate based on G_I is expected to be larger for the smaller delamination. As pointed out previously, the distributions of G_{II} for circular and elliptical delaminations are quite different. Even the location of maximum G_{II} is different. The peak values of G_{II} for the two delaminations are similar. Therefore, based on G_{II}, the growth rate should be about the same for both delaminations, but the direction of growth would be different.

Conclusions

A three-dimensional, geometrically nonlinear, finite element program, NONLIN3D, was developed to calculate the strain-energy release rate components for a postbuckled embedded delamination. The program NONLIN3D uses substructuring to reduce the number of equations which must be solved iteratively. A new technique was developed for calculating strain-energy release rates G_I, G_{II}, and G_{III}. This technique is based on virtual crack closure. Various checks of NONLIN3D and the finite element

models were performed to establish confidence in the results presented herein. A parametric study was performed for postbuckled elliptical delaminations in a "homogeneous quasi-isotropic laminate." Based on the parametric analysis, the following conclusions were reached:

1. The problem is definitely mixed-mode. In some cases, G_I is larger than G_{II}; for other cases, the opposite is true.
2. In general, there is a large gradient in the strain-energy release rates along the delamination front.
3. The locations of maximum G_I and G_{II} depend on the delamination shape and the applied strain.
4. The mode III component was negligible for all cases considered.
5. The analysis predicted that parts of the delamination would overlap. The analysis presented herein does not impose contact constraints to prevent this overlapping. Further work is needed to determine the effect of allowing the overlapping.

NASA Langley Research Center
Hampton, Virginia 23665-5225
May 26, 1988

References

1. Whitcomb, John D.: Finite Element Analysis of Instability Related Delamination Growth. *J. Compos. Mater.*, vol. 15, Sept. 1981, pp. 403–426.
2. Whitcomb, John D.: Approximate Analysis of Postbuckled Through-Width Delaminations. *Compos. Technol. Review,* vol. 4, no. 3, Fall 1982, pp. 71–77.
3. Whitcomb, John D.: Strain-Energy Release Rate Analysis of Cyclic Delamination Growth in Compressively Loaded Laminates. *Effects of Defects in Composite Materials.* ASTM STP 863, American Soc. for Testing & Materials, c.1984, pp. 175–193.
4. Whitcomb, John D.: Parametric Analytical Study of Instability-Related Delamination Growth. *Compos. Sci. & Technol.,* vol. 25, no. 1, 1986, pp. 19–48.
5. Chai, Herzl; Babcock, Charles D.; and Knauss, Wolfgang G.: One Dimensional Modelling of Failure in Laminated Plates by Delamination Buckling. *Int. J. Solids & Struct.,* vol. 17, no. 11, 1981, pp. 1069–1083.
6. Ashizawa, M.: Fast Interlaminar Fracture of a Compressively Loaded Composite Containing a Defect. *Proceedings of the Fifth DOD/NASA Conference on Fibrous Composites in Structural Design, Volume 1,* NASA Ames Research Center, 1981, pp. 1–269—1–292. (Available from DTIC as AD B060 752L.)
7. Ramkumar, R. L.: *Fatigue Degradation in Compressively Loaded Composite Laminates.* NASA CR-165681, 1981.
8. Ramkumar, R. L.: *Performance of a Quantitative Study of Instability-Related Delamination Growth.* NASA CR-166046, 1983.
9. Gillespie, J. W., Jr.; and Pipes, R. B.: Compressive Strength of Composite Laminates With Interlaminar Defects. *Compos. Struct.,* vol. 2, no. 1, 1982, pp. 49–69.
10. Chai, Herzl; and Babcock, Charles D.: Two-Dimensional Modelling of Compressive Failure in Delaminated Laminates. *J. Compos. Mater.,* vol. 19, Jan. 1985, pp. 67–98.
11. Fei, Zhizhong; and Yin, Wan-Lee: Postbuckling Growth of a Circular Delamination in a Laminate Under Compression and Bending. Georgia Inst. of Technology paper presented at the Twelfth Southeastern Conference on Theoretical and Applied Mechanics (Pine Mountain, Georgia), May 10–11, 1984.
12. Konishi, D. Y.; and Johnston, W. R.: Fatigue Effects on Delaminations and Strength Degradation in Graphite/Epoxy Laminates. *Composite Materials: Testing and Design (Fifth Conference),* S. W. Tsai, ed., ASTM STP 674, American Soc. for Testing & Materials, c.1979, pp. 597–619.
13. Shivakumar, K. N.; and Whitcomb, J. D.: Buckling of a Sublaminate in a Quasi-Isotropic Composite Laminate. *J. Compos. Mater.,* vol. 19, Jan. 1985, pp. 2–18.
14. Whitcomb, John D.; and Shivakumar, K. N.: Strain-Energy Release Rate Analysis of a Laminate With a Postbuckled Delamination. *Numerical Methods in Fracture Mechanics,* A. R. Luxmoore, D. R. J. Owen, Y. P. S. Rajapakse, and M. F. Kanninen, eds., Pineridge Press (Swansea, United Kingdom), c.1987, pp. 581–605. (Available as NASA TM-89091, 1987.)
15. Webster, John D.: *Flaw Criticality of Circular Disbond Defects in Compressive Laminates—1980–81 Interim Report.* CCM-81-03 (Grant 1304), Center for Composite Materials, Univ. of Delaware, June 1981. (Available as NASA CR-164830.)
16. Chai, H.; Knauss, W. G.; and Babcock, C. D.: Observation of Damage Growth in Compressively Loaded Laminates. *Exp. Mech.,* vol. 23, no. 3, Sept. 1983, pp. 329–337.
17. Byers, Bruce A.: *Behavior of Damaged Graphite/Epoxy Laminates Under Compression Loading.* NASA CR-159293, 1980.
18. Porter, T. R.: *Compression and Compression Fatigue Testing of Composite Laminates.* NASA CR-168023, 1982.
19. Frederick, Daniel; and Chang, Tien Sun: *Continuum Mechanics.* Scientific Publ., Inc., 1972, pp. 79–82.
20. Weaver, William, Jr.: *Computer Programs for Structural Analysis.* D. Van Nostrand Co., Inc., c.1967.
21. Rybicki, E. F.; and Kanninen, M. F.: A Finite Element Calculation of Stress Intensity Factors by a Modified Crack Closure Integral. *Eng. Fract. Mech.,* vol. 9, no. 4, 1977, pp. 931–938.

22. Raju, I. S.; and Newman, J. C., Jr.: Stress-Intensity Factors for a Wide Range of Semi-Elliptical Surface Cracks in Finite-Thickness Plates. *Eng. Fract. Mech.*, vol. 11, no. 4, 1979, p. 819.
23. Wang, S. S.; and Choi, I.: *The Mechanics of Delamination in Fiber-Reinforced Composite Materials. Part I—Stress Singularities and Solution Structure.* NASA CR-172269, 1983.
24. Timoshenko, S.; and Woinowsky-Krieger, S.: *Theory of Plates and Shells,* Second ed. McGraw-Hill Book Co., Inc., 1959, pp. 415–416.

Table 1. Statistics on Models Used in Convergence Study

[Substructures 1 and 2 are linear and nonlinear, respectively]

Model	Number of nodes/Number of elements				Number
	2-D model	3-D model	Substructure 1	Substructure 2	
1	143/36	1719/288	1475/256	287/32	8
2	153/38	1841/304	1475/256	409/48	8
3	173/42	1129/168	799/128	353/40	4
4	173/42	2085/336	1475/256	653/80	8
5	173/42	3041/504	2151/384	953/120	12
6	533/152	6325/1216	5173/1024	1221/192	8

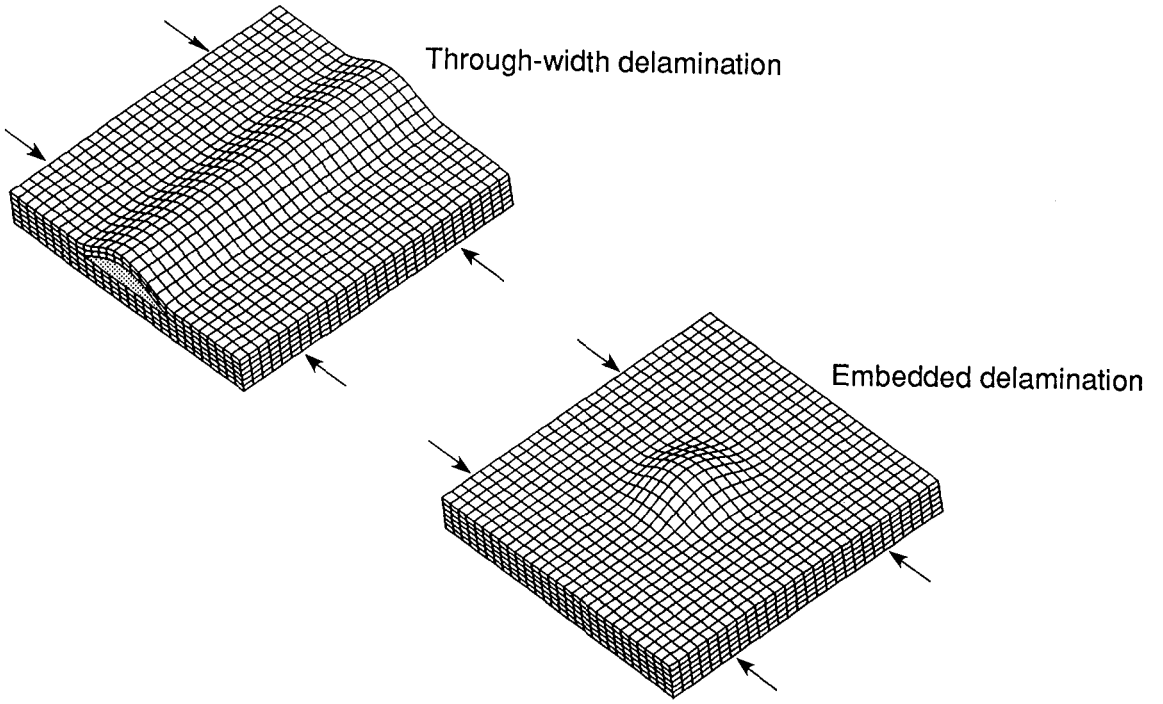

Figure 1. Two configurations which exhibit instability-related delamination growth.

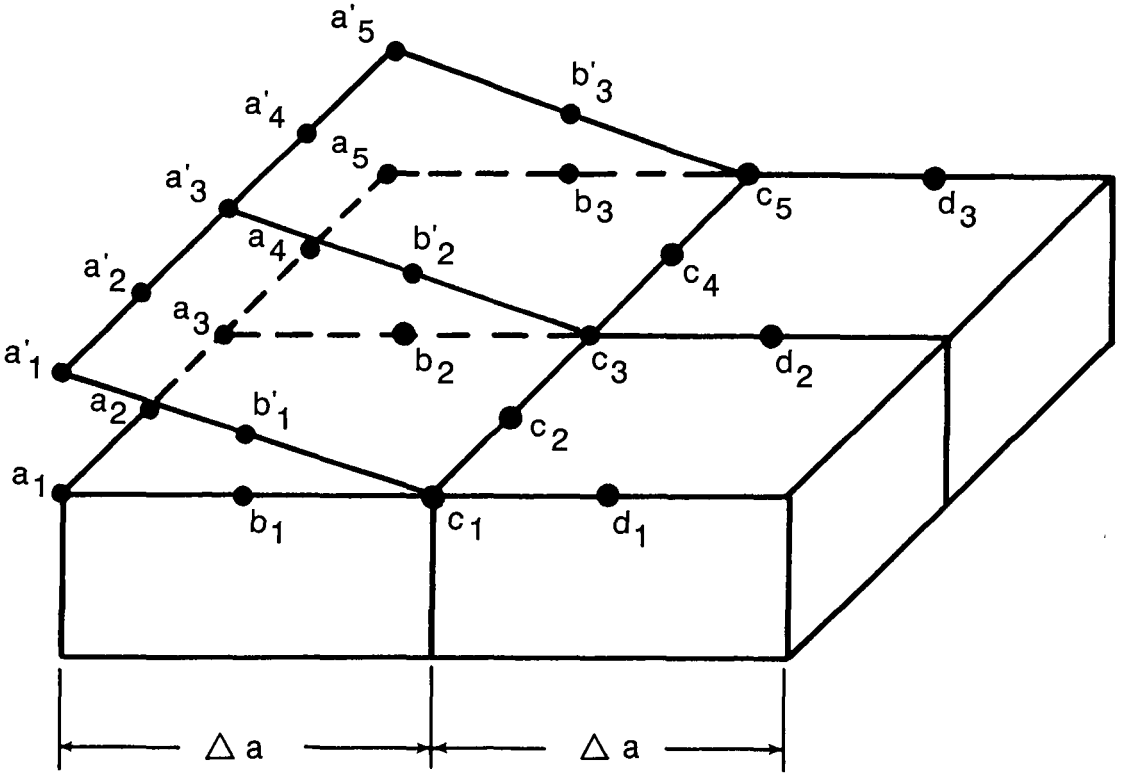

Figure 2. Schematic of delamination front region.

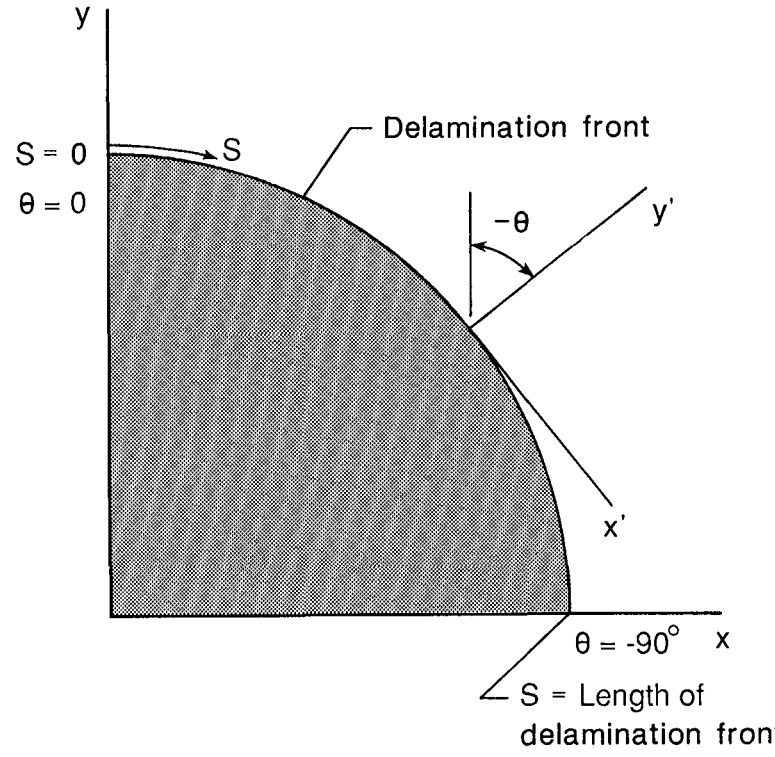

Figure 3. Global and local coordinate systems and perimeter coordinate S.

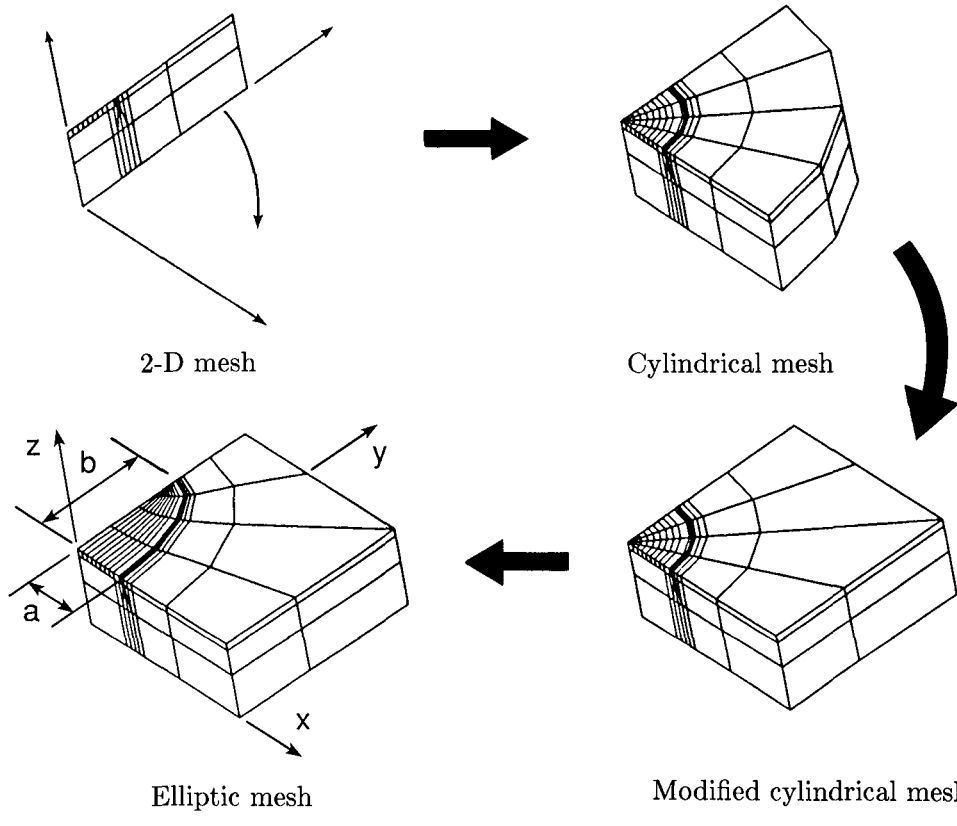

Figure 4. Procedure of generating three-dimensional finite element models.

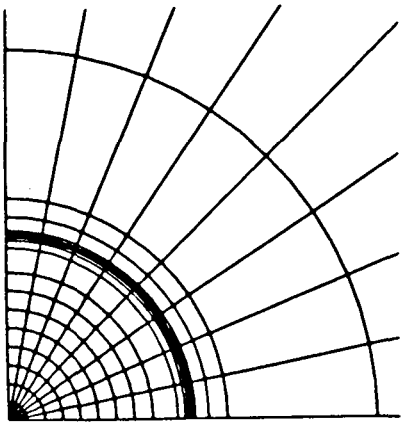

(a) Before transformation.

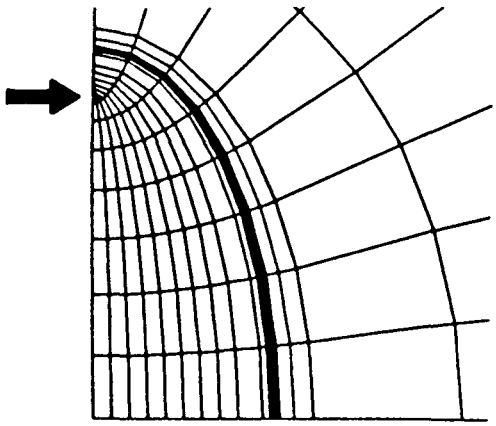

(b) After elliptic transformation.

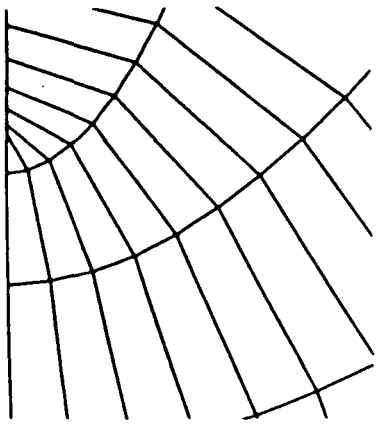

(c) Close-up of region indicated by arrow in (b).

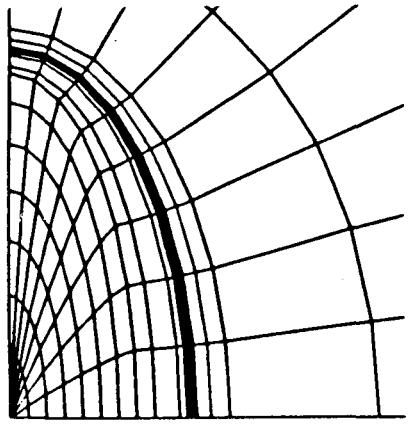

(d) After modified elliptic transformation.

Figure 5. Transformed meshes using elliptic transformation of reference 22 and the modified transformation.

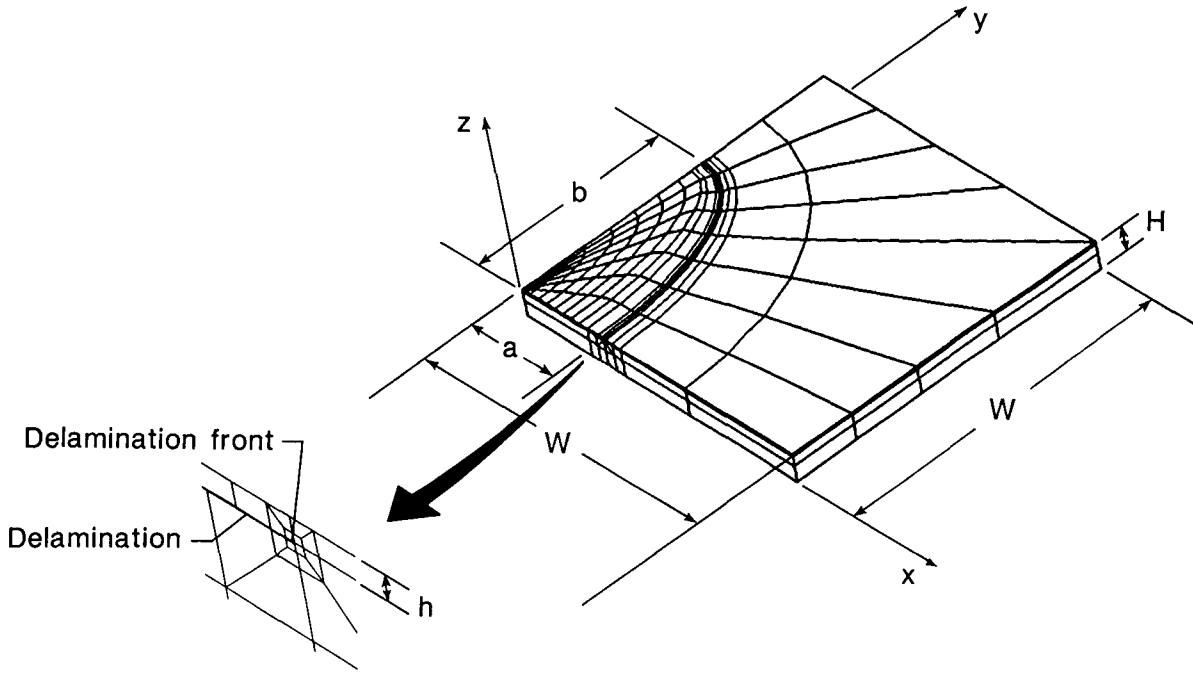

Figure 6. Typical finite element model.

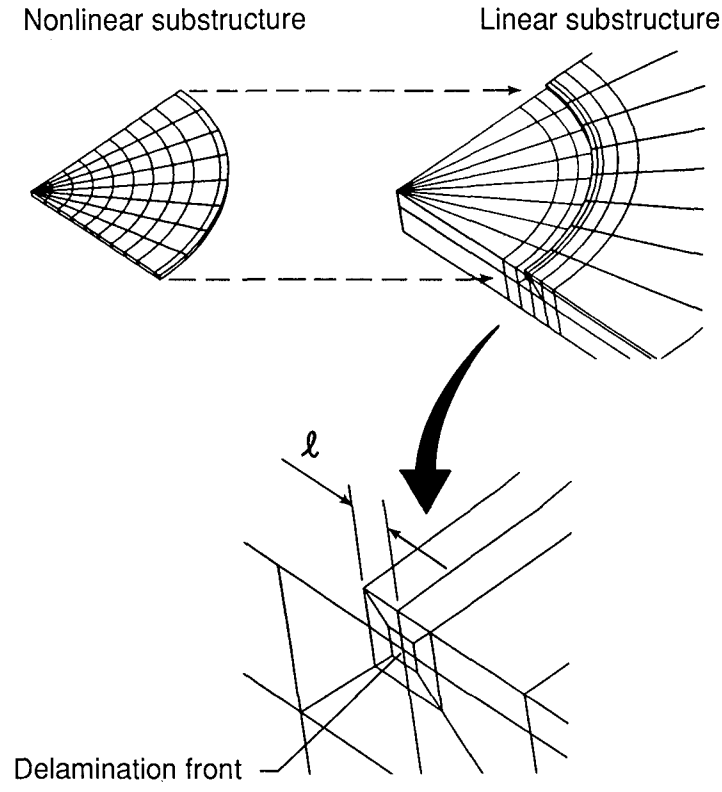

Figure 7. Typical division of model into substructures.

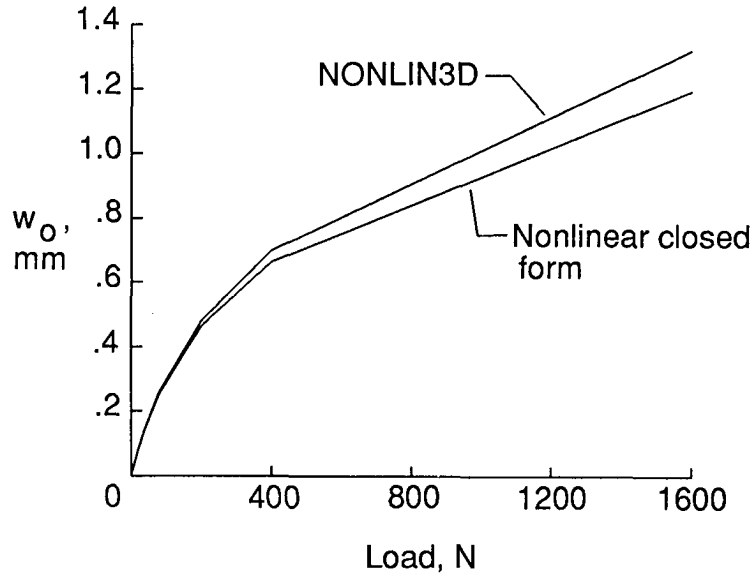

(a) Deflection.

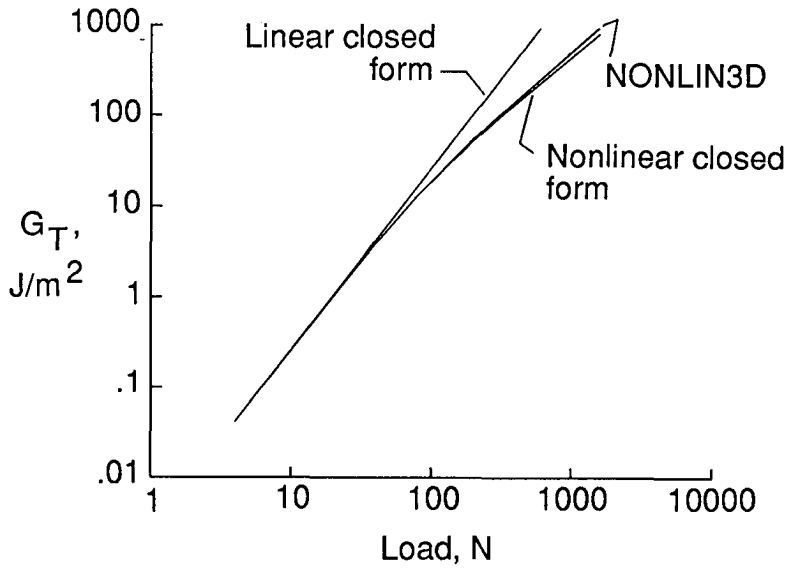

(b) Total strain-energy release rate.

Figure 8. Analysis of transversely loaded plate with circular delamination.

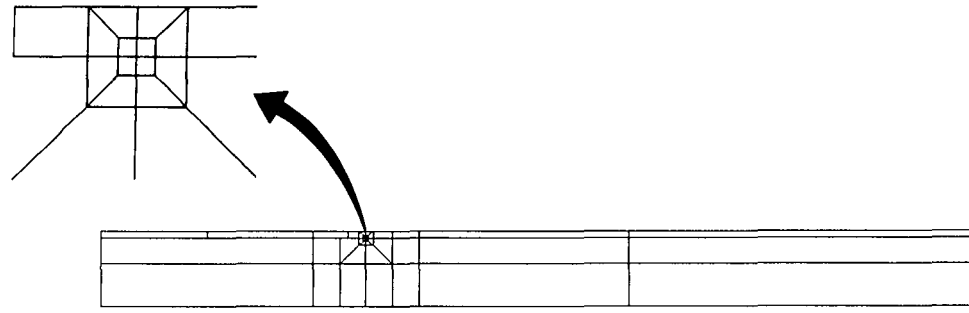

(a) Coarse 2-D model which has 143 nodes.

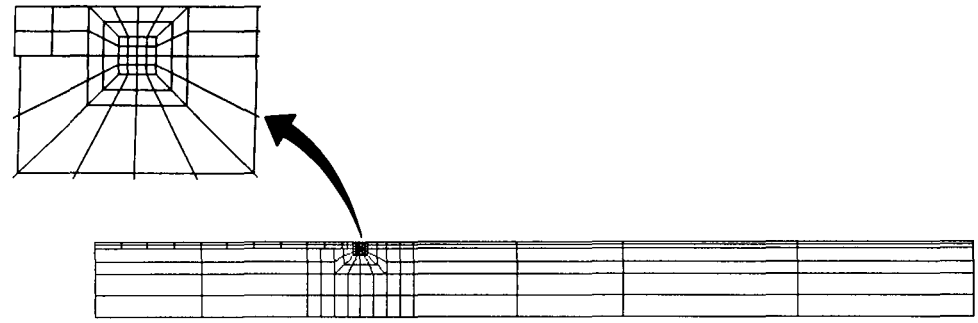

(b) Refined 2-D model which has 533 nodes.

Figure 9. Range of two-dimensional mesh refinement for convergence study.

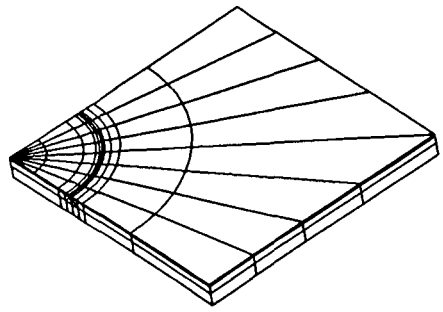

(a) Model 1.

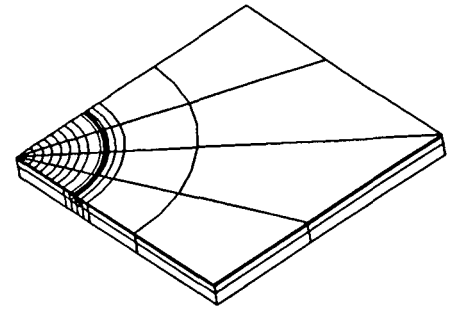

(b) Model 3.

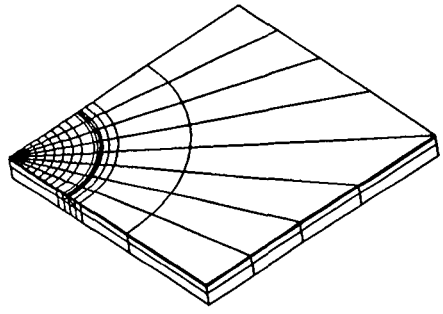

(c) Model 4.

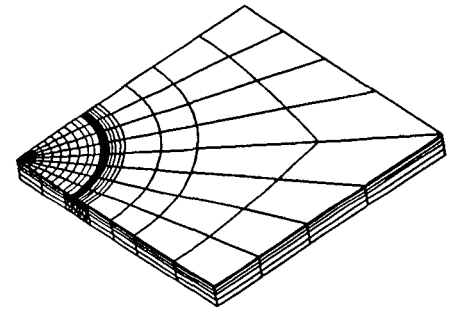

(d) Model 6.

Figure 10. Several of the three-dimensional meshes used in convergence study.

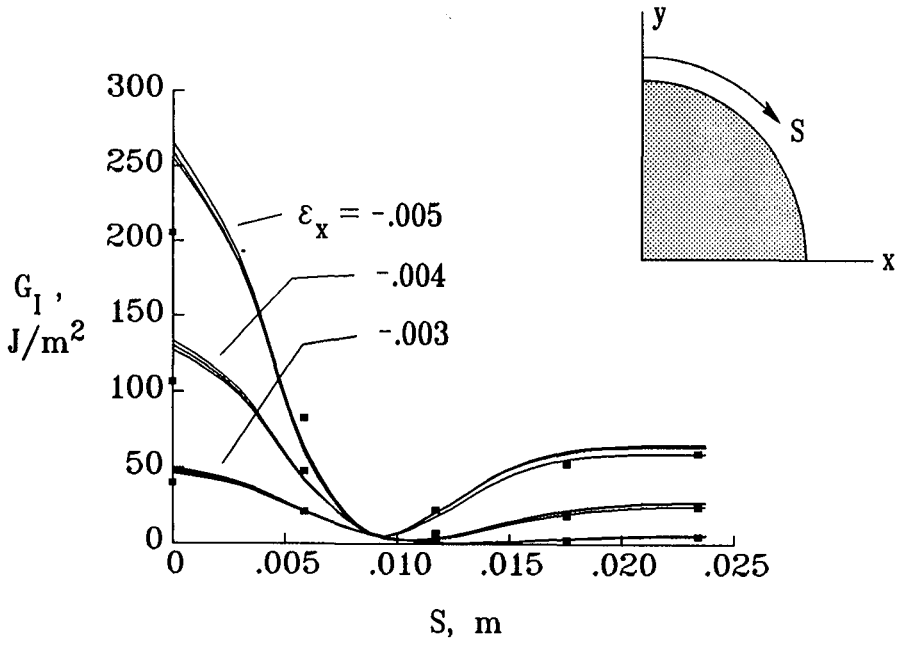

(a) Mode I.

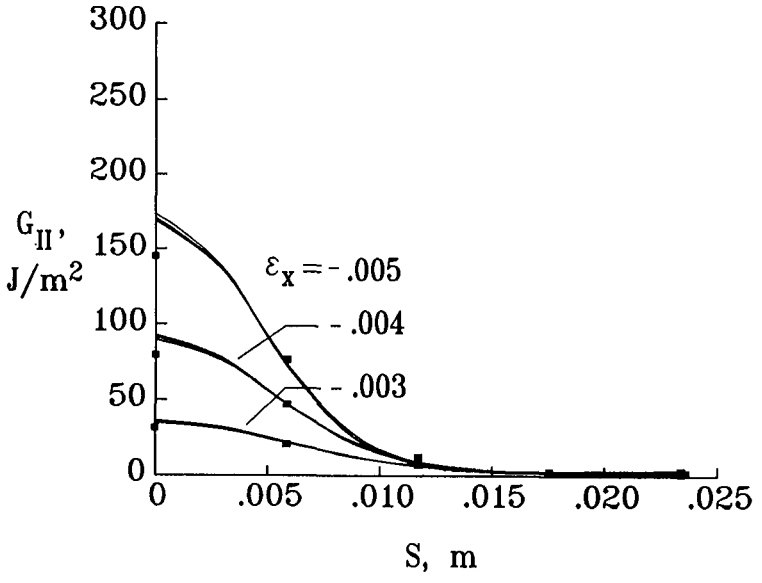

(b) Mode II.

Figure 11. Strain-energy release rates calculated using different meshes.

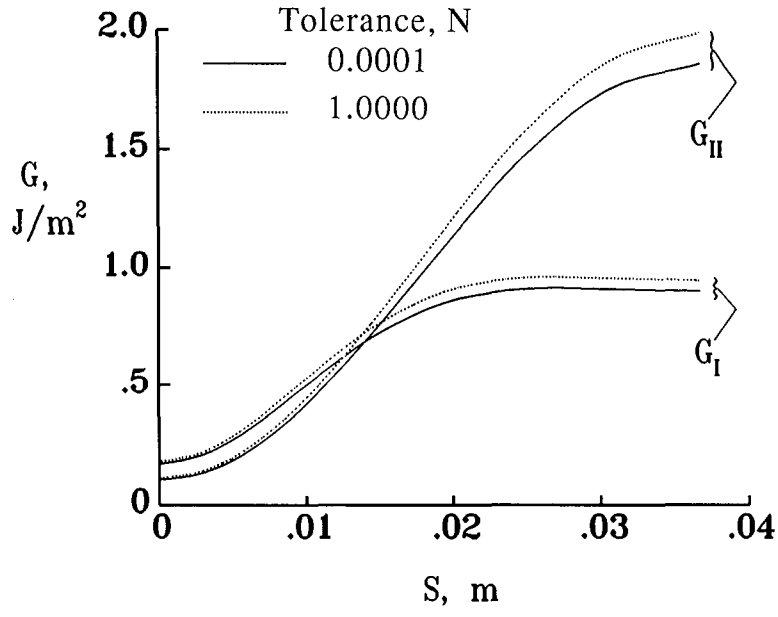

Figure 12. Effect of specified residual tolerance on G_I and G_{II}. Applied strain = −0.001.

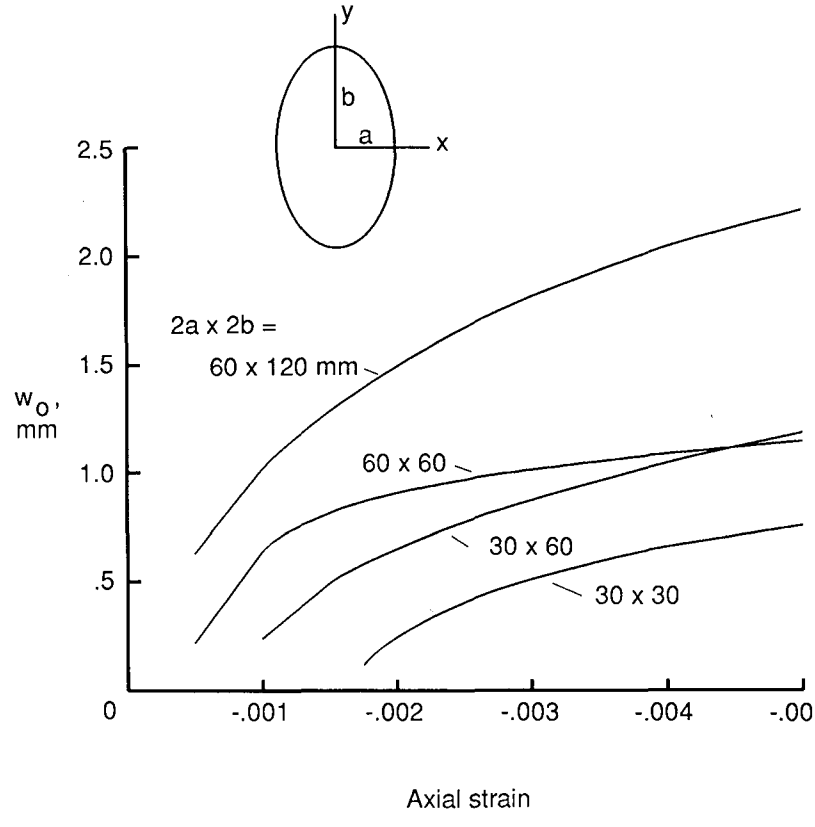

Figure 13. Peak transverse displacement versus axial strain for four delamination sizes.

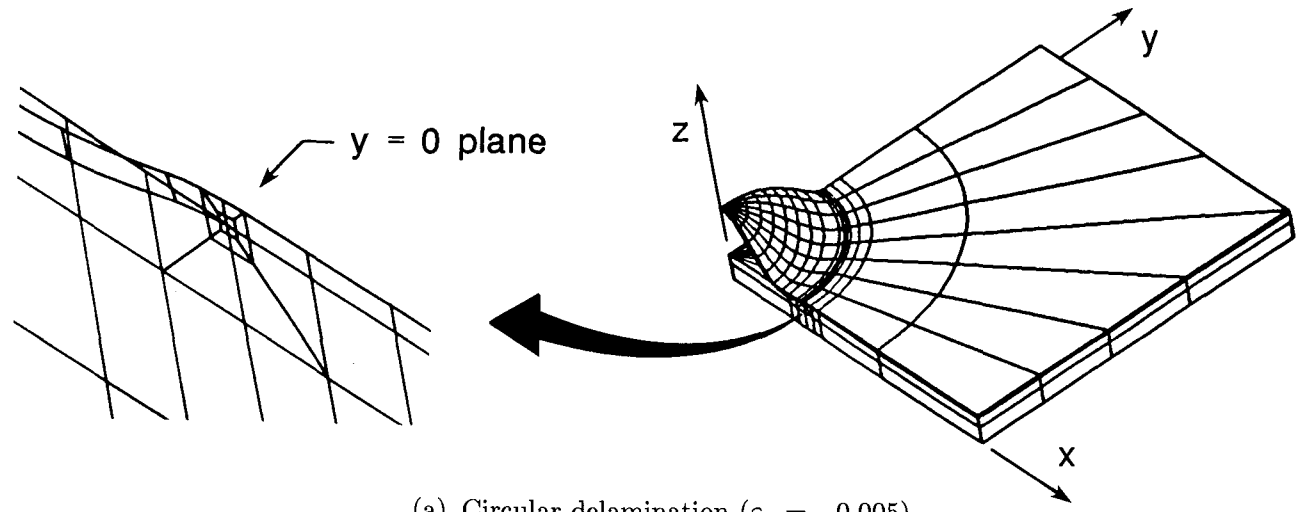

(a) Circular delamination ($\varepsilon_x = -0.005$).

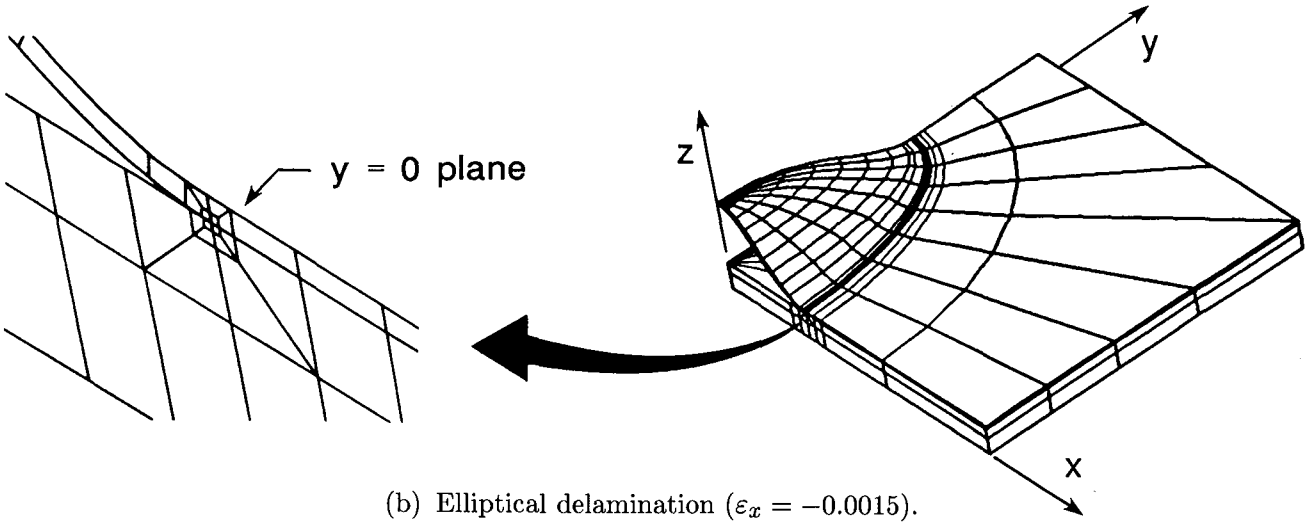

(b) Elliptical delamination ($\varepsilon_x = -0.0015$).

Figure 14. Deformed finite element models for two configurations.

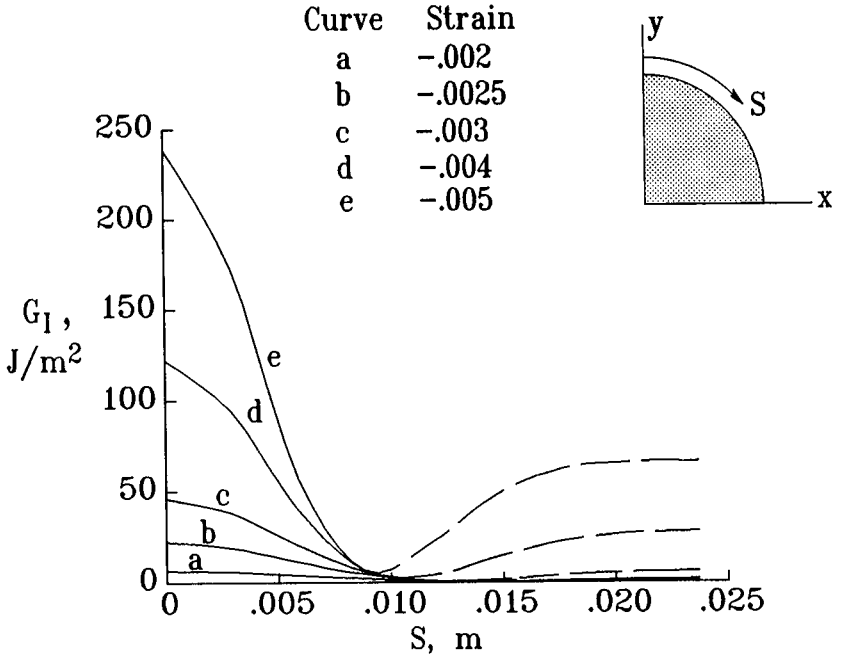

(a) Mode I.

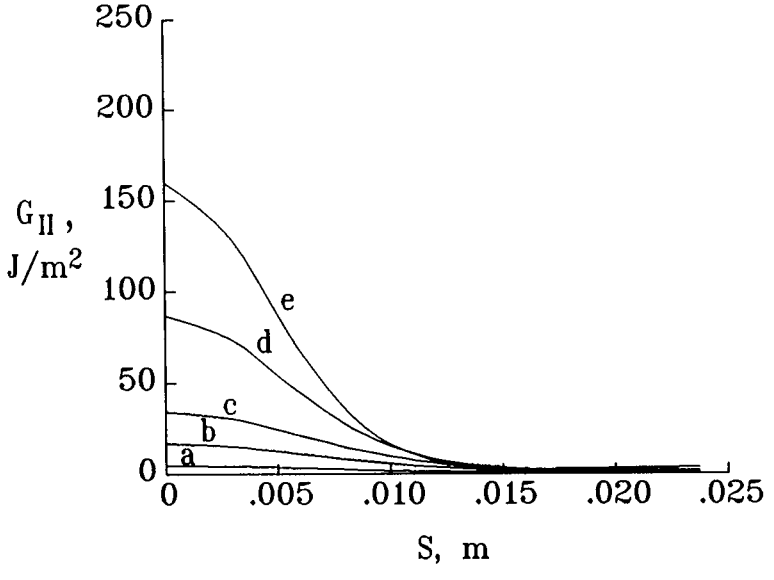

(b) Mode II.

Figure 15. Strain-energy release rate distributions for a circular delamination. (Diameter = 30 mm.) Dashed lines indicate overlapping.

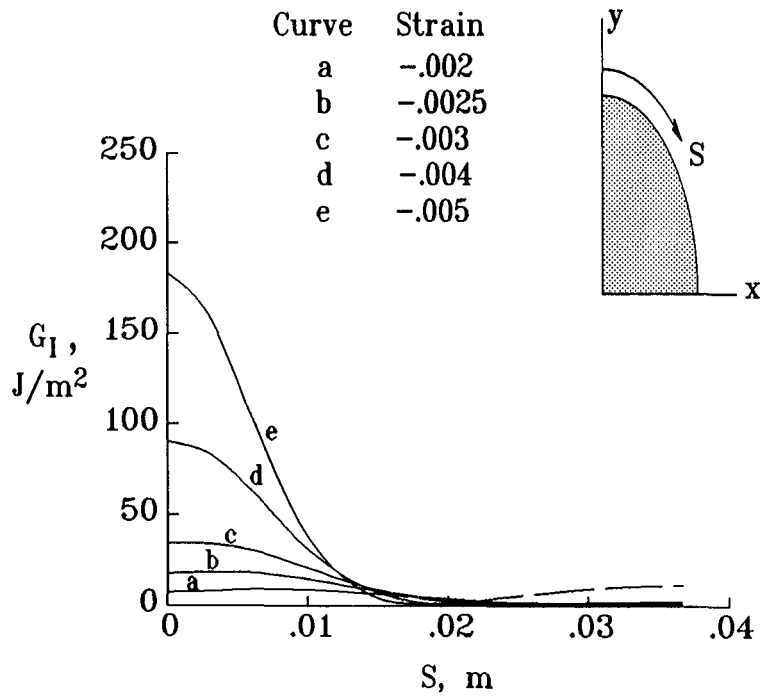

(a) Mode I.

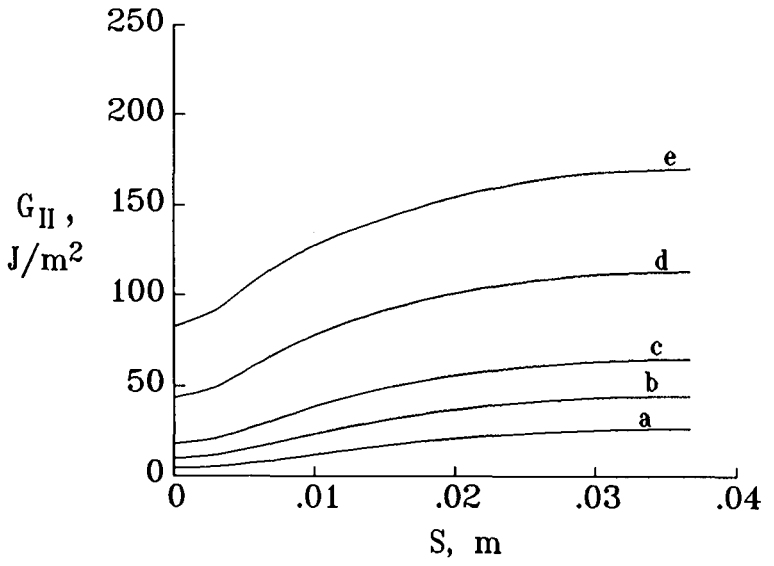

(b) Mode II.

Figure 16. Strain-energy release rate distributions for an elliptical delamination. ($2a \times 2b = 30 \times 60$ mm.) Dashed lines indicate overlapping.

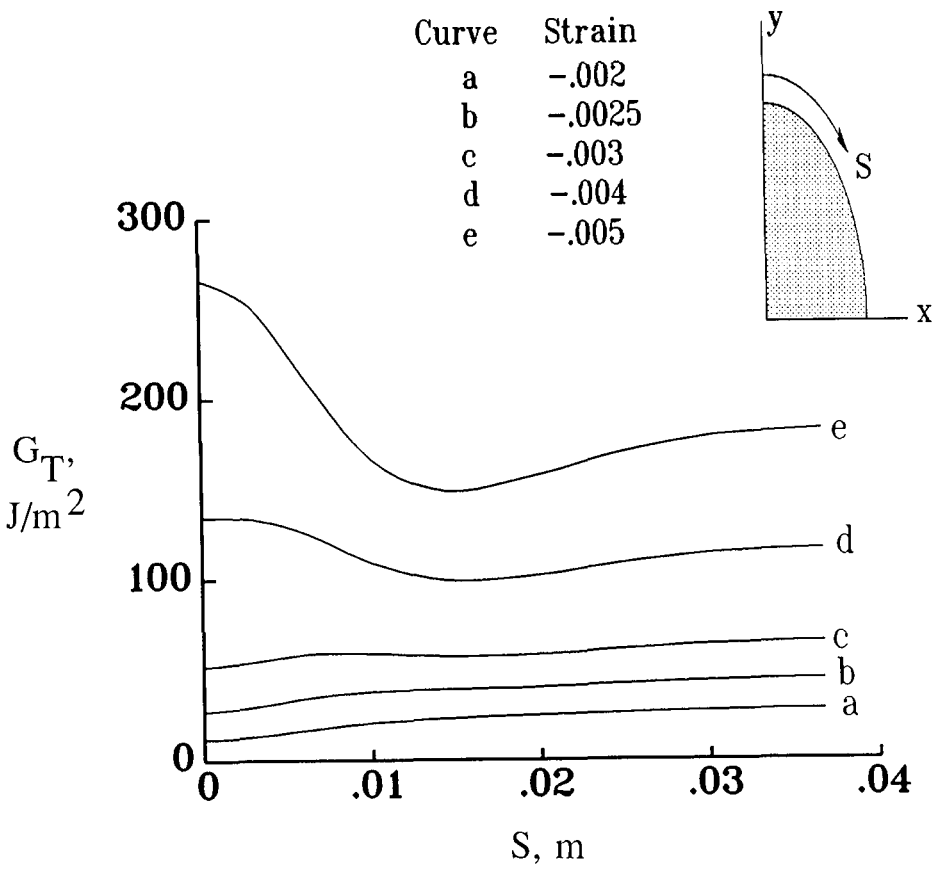

(c) Total strain-energy release rate.

Figure 16. Concluded.

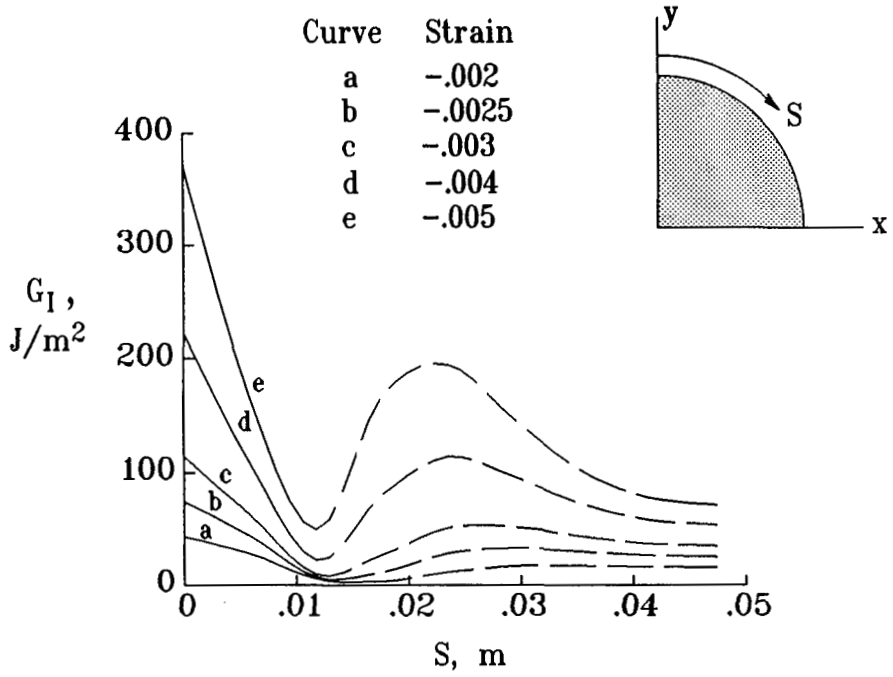

(a) Mode I.

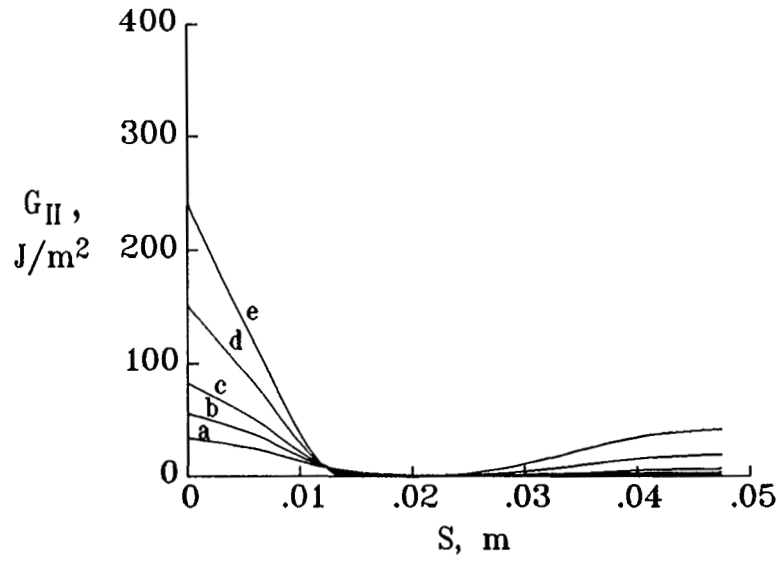

(b) Mode II.

Figure 17. Strain-energy release rate distributions for a circular delamination. (Diameter = 60 mm.) Dashed lines indicate overlapping.

NASA
National Aeronautics and Space Administration

Report Documentation Page

1. Report No.	2. Government Accession No.	3. Recipient's Catalog No.
NASA TP-2823		

4. Title and Subtitle	5. Report Date
Three-Dimensional Analysis of a Postbuckled Embedded Delamination	July 1988
	6. Performing Organization Code
7. Author(s)	8. Performing Organization Report No.
John D. Whitcomb	L-16453
9. Performing Organization Name and Address	10. Work Unit No.
NASA Langley Research Center Hampton, VA 23665-5225	505-63-01-05
	11. Contract or Grant No.
12. Sponsoring Agency Name and Address	13. Type of Report and Period Covered
National Aeronautics and Space Administration Washington, DC 20546-0001	Technical Paper
	14. Sponsoring Agency Code

15. Supplementary Notes

16. Abstract

Delamination growth caused by local buckling of a delaminated group of plies was investigated. Delamination growth was assumed to be governed by the strain-energy release rates G_I, G_{II}, and G_{III}. The strain-energy release rates were calculated using a geometrically nonlinear, three-dimensional, finite element analysis. The program is described and several checks of the analysis are discussed. Based on a limited parametric study, the following conclusions were reached:

1. The problem is definitely mixed-mode. In some cases G_I is larger than G_{II}; for other cases the opposite is true.
2. In general, there is a large gradient in the strain-energy release rates along the delamination front.
3. The locations of maximum G_I and G_{II} depend on the delamination shape and the applied strain.
4. The mode III component was negligible for all cases considered.
5. The analysis predicted that parts of the delamination would overlap. The results presented herein did not impose contact constraints to prevent overlapping. Further work is needed to determine the effects of allowing the overlapping.

17. Key Words (Suggested by Authors(s))	18. Distribution Statement
Buckling Local buckling Compression Delamination Strain-energy release rate	Unclassified—Unlimited Subject Category 24

19. Security Classif.(of this report)	20. Security Classif.(of this page)	21. No. of Pages	22. Price
Unclassified	Unclassified	25	A02

NASA FORM 1626 OCT 86 NASA-Langley, 1988

For sale by the National Technical Information Service, Springfield, Virginia 22161-2171

National Aeronautics and
Space Administration
Code NTT-4

Washington, D.C.
20546-0001

NASA